Non-Gaussian Concentration Profile of Hydrogen Diffused in the Zinc Oxide Bulk Crystal

R. Jakieła* and A. Barcz

Institute of Physics, Polish Academy of Sciences, al. Lotników 32/46, PL-02688 Warszawa, Poland

Received: 20.10.2025 & Accepted: 10.12.2025

Doi: 10.12693/APhysPolA.148.267 *e-mail: jakiela@ifpan.edu.pl

Hydrogen in ZnO is characteristic for its by high mobility and limited solubility; consequently, the classical Gaussian broadening expected for diffusion from a localized source is not observed after post-implantation annealing. In this work, c-axis ZnO single crystals were implanted with 1 MeV H^+ (fluence 1×10^{16} cm^{-2}), annealed in flowing O_2 at 300°C and 600°C for 15–30 min, and their depth profiles were quantified by secondary ion mass spectrometry. The profiles were observed to evolve in a non-Gaussian manner. At 300°C the peak narrows and increases, whereas at 600°C the near-peak region is depleted. A long, asymmetric tail and a surface-proximal excess are developed, indicating that rapid out-diffusion, trapping, and limited solubility govern the evolution rather than Fickian spreading. The diffusion coefficient D at 600°C was extracted directly from the difference between the initial and annealed profiles. A semi-infinite model with an absorbing surface, with no need to assume a Gaussian initial profile, was applied. Reduction in the overall content after 15 and 30 min at 600°C yields the value of $D = 6 \times 10^{-9}$ cm^2/s. These results provide a consistent framework for extracting diffusion parameters from non-Gaussian profiles in hydrogenated ZnO, highlighting the dominant role of surface exchange, trapping, and low equilibrium solubility in shaping the measured hydrogen distributions.

topics: diffusion, hydrogen, ZnO, secondary ion mass spectrometry (SIMS)

1. Introduction

Zinc oxide is a wide direct bandgap II–VI compound semiconductor (E_g = 3.37 eV at room temperature) with the wurtzite crystal structure. ZnO shows several advantages over GaN, including a larger free exciton binding energy (60 meV versus 26 meV for GaN), which makes this material suitable for ultraviolet/visible (UV/VIS) optoelectronics and transparent electronics. The optical properties of ZnO make this semiconductor a promising candidate for short-wavelength optical devices such as light-emitting diodes (LEDs) or laser diodes (LDs). Hydrogen acts as a shallow donor in ZnO, a point first established theoretically and then verified experimentally [1, 2]. Already the earliest observations linked hydrogenation with increased conductivity and characteristic changes in luminescence [3, 4]. Usually, two dominant configurations are considered, namely interstitial H (H_i) and substitutional H on the oxygen site (H_O) — both act as shallow donors in their stable charge states [5, 6]. A direct way to identify the defect states (with H-related centers) is to study fingerprints of local vibrations [7]; most frequently studied is the O–H stretch near 3611 cm^{-1}. Muonium (a light-mass analogue of the hydrogen atom) provides a clean experimental confirmation of a hydrogenic shallow level, consistent with the donor model [2].

First-principles work clarified the site energetics and the role of the Fermi level, predicting charge-state transitions and site preferences for H_i and H_O [8]. Hydrogen readily passivates acceptors, reducing compensation and boosting mobility, which helps explain the unintentional n-type behavior in nominally undoped ZnO [9]. Ion implantation studies have shown that large, near-surface H accumulation can drive a significant conductivity increase by forming donor-like OH complexes [10]. Nuclear magnetic resonance (NMR) and related techniques resolve multiple motional processes of interstitial protons at low activation energies, consistent with fast local reorientation and hopping [11]. Beyond isolated donors, hydrogen binds to intrinsic defects (e.g., vacancies), modifying electronic levels and sometimes creating metastable states that influence persistent photoconductivity and doping limits [8]. In ALD-grown ZnO films (here, ALD

— atomic layer deposition), isotope-resolved SIMS (secondary ion mass spectrometry) shows that the most unintentional H comes from the metalorganic Zn precursor (DEZn). In contrast, weakly bound OH derived from the water precursor is primarily removed by a 3-minute rapid thermal processing (RTP) anneal at 800°C [12].

The overall picture is that hydrogen in ZnO creates a tunable, defect-sensitive donor system whose spectroscopic, electrical, and thermodynamic properties depend on the preparation method, Fermi level, and coexisting defects.

Direct depth profiling after low-temperature hydrogenation revealed very fast indiffusion with small apparent activation energies — classically modeled by the semi-infinite complementary-error-function solution [13, 14]. Previous work established the basic SIMS methodology and source-limited kinetics, including deuterium markers and calibration strategies crucial for sample comparison [15, 16]. Plasma exposure combined with annealing demonstrated that hydrogen uptake in ZnO is governed by near-surface incorporation processes, while the subsequent transport into the bulk is rapid, indicating that the overall incorporation rate is limited by surface exchange rather than bulk diffusion [17, 18].

Atomistic theory places the intrinsic H_i migration barrier at around 0.4–0.5 eV, which is consistent with high mobility even at near-room temperature [19, 20]. When traps are present, macroscopic fits require trapping/detrapping terms, which yields larger *effective* activation energy E_a and prefactors than the intrinsic hop would imply [21, 22]. In hydrothermal single crystals, H-implanted profiles and annealing transients are reproduced only by trap-limited models with E_a near 0.8–1.0 eV. In thin polycrystalline films, the microstructure dominates; grain boundaries and porosity provide pathway for H_2, leading to higher apparent barriers and a broad spread of the diffusivity $D(T)$ [9, 23]. Surface exchange can be the rate-limiting step; TPD/XPS-style measurements separate surface OH loss from bulk H evolution, helping to deconvolution proper diffusion from the injection [24] (here, TPD — temperature programmed desorption; XPS — X-ray photoelectron spectroscopy). Resistometry and in-situ transport indicate anisotropy — faster along the c axis than along the a axis — consistent with open wurtzite channels [25, 26]. The film-growth route and defect inventory shift the dominant carrier between atomic H and molecular H_2, changing both apparent E_a and time constants [27, 28]. Post-implant evolution reveals electrically active n^+ layers that relax via dissociation of immobile complexes rather than simple Gaussian broadening, indicating the presence of traps [29, 30]. A kinetically stable "hidden-H_2–V_O" reservoir can feed or deplete the mobile H_i population upon thermal cycling, reconciling fast diffusion with long-lived donor activity [31]. Hydrothermal H- and ^{2}H-implanted ZnO exhibits diffusion and activation governed by defect reactions, where H passivates Li_{Zn} acceptors as neutral (H–Li_{Zn}) complexes [32]. Under these conditions, only 1–2% of the implanted H is donor-active, with the rest trapped in complexes (including H_2–V_{Zn}) or bubbles.

We investigate hydrogen-implanted ZnO subjected to post-implantation annealing. Owing to the exceptionally high mobility of interstitial H and its low equilibrium solubility in ZnO, the redistribution is dominated by rapid out-diffusion, trapping, and effusion rather than by simple self-similar Fickian broadening. As a result, the depth profile does not evolve toward the classical Gaussian distribution expected for diffusion from a localized source. Instead, it exhibits near-peak depletion with non-Gaussian tails set by surface exchange and trap-limited kinetics.

2. Experiment

C-oriented [0001], one-side-polished ZnO bulk crystals were used for implantation. H^+ implantations were conducted at room temperature (RT) using a NEC 3SDH-2 Pelletron tandem accelerator. Samples were tilted by 7° with respect to the ion beam axis to prevent ion channeling. Irradiation was carried out with an energy of 1 MeV to a fluence of 1×10^{16} cm^{-2}. The thus implanted hydrogen, with a maximum concentration of atoms at a depth of 9.2 μm, serves as a diffusion source for further processing. Post-implantation thermal annealing was performed using an RTP furnace in flowing oxygen at atmospheric pressure, for 15 and 30 min, at temperatures of 300°C and 600°C. Hydrogen concentration profiles were measured using a SIMS Cameca IMS 6F microanalyzer with a Cs mass-filtered primary ion beam at a voltage of 15 keV and an intensity of 150 nA. The beam was focused into a spot $\sim$ 30 μm in diameter and rastered over a nominal area of 100×100 μm^2. The selected probing field was 30 μm in diameter, centered in the crater. Since the detectability of "ambient" species is limited mainly by the rate of their adsorption on the sample surface, care was taken to minimize the residual pressure. Under these conditions, the pressure in the sample chamber amounted to (1–1.5) $\times 10^{10}$ Torr with the beam on. The concentration of hydrogen species in the as-implanted and annealed samples was calculated using the appropriate standard as described in [33].

3. Results and discussion

Accurate diffusion coefficients, i.e., pre-exponents D_0 and activation energies E_a, govern the rates and length scales of mass transport, thereby setting the time-temperature windows for processes such

TABLE I

Diffusion parameters from different sources and diffusion coefficients calculated for 300°C and 600°C.

Paper / Figure	D_0 [cm^2/s]	E_{a} [eV]	D at 300°C [cm^2/s]	D at 600°C [cm^2/s]
[34] / 1	2.5×10^{-2}	0.85 ± 0.19	8.35×10^{-10}	3.09×10^{-7}
[15] / 2	2.5×10^{-8}	0.17 ± 0.12	8.0×10^{-10}	2.61×10^{-9}

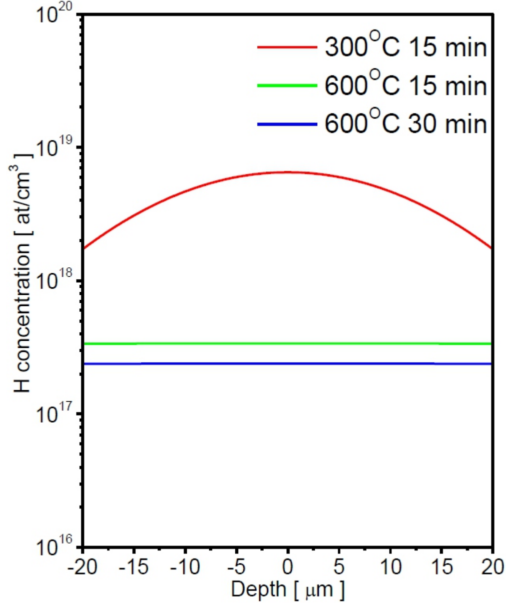

Fig. 1. Hydrogen diffusion concentration profiles for the highest diffusion coefficient, as calculated based on results from [34].

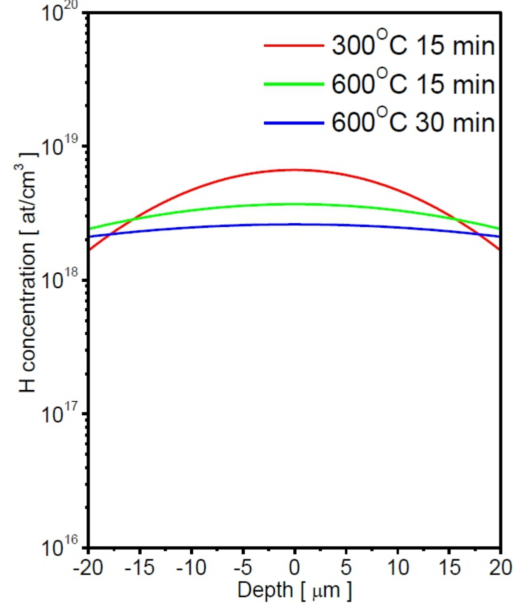

Fig. 2. Hydrogen diffusion concentration profiles for the lowest diffusion coefficient, as calculated based on results from [15].

as doping, sintering, aging, corrosion, and interdiffusion. Reliable data on temperature-dependent diffusion coefficient $D(T)$ enable predictive control of concentration profiles and microstructures, robust process scale-up, and physics-based lifetime simulations under thermal or electrical stress. Without validated diffusivities, designs risk unintended gradients, phase changes, and reliability loss; precise measurement and modeling of diffusion under realistic boundary conditions are therefore fundamental to process control, defect engineering, and long-term material stability.

Previous results of diffusion coefficient parameters, obtained using monocrystalline ZnO bulk material, mostly showed activation energy E_a in the range 0.17–0.85 eV [15, 21, 24, 34]. These values agreed with theoretical calculations based on first principles, which provide values of 0.4–0.5 eV [19, 20]. All experimental data were taken using either an infinite or semi-infinite source of diffused hydrogen. Moreover, only two papers develop a pre-exponential factor D_0 for the diffusion coefficient — unfortunately, with widely diverging values of 2.5×10^{-8} cm^2/s [15] and 2.5×10^{-2} cm^2/s [34]. A similar value of the parameter D_0 of 3×10^{-2} cm^2/s was demonstrated in a very early work by Thomas and Lander [4], using the ZnO bulk material in the form of needles. It is worth noting that diffusion from a finite source, with determination of diffusion parameters, had not been previously performed.

To compare previous results with the current research, a simulation of diffusion process was provided taking into account the highest [34] and the lowest [15] diffusion coefficients at experimental temperatures of 300°C and 600°C. The diffusion coefficient parameters and the final diffusion coefficient at specific temperatures are listed in Table I, while the concentration profiles are illustrated in Figs. 1 and 2.

The diffusion concentration profiles were calculated using

$$C\left(x,t\right)=\frac{Q}{\sqrt{\pi Dt}}\ \exp\left(-\frac{x^2}{4Dt}\right), \tag{1}$$

where Q is the fluence. Note that the Q values from the current experiment were used in the simulations.

The profiles presented in Figs. 1 and 2 indicate that, considering the highest diffusion coefficient, the concentration profiles after annealing at 600°C should be completely flat in the depth

range studied. Furthermore, taking into account the non-delta initial concentration profile, with the maximum at a particular depth determined by the range of implantation, the resultant Gaussian concentration profile should be calculated using

$$C\left(x,t\right)=\frac{Q}{\sqrt{\pi D\,t}}\;\exp\left(-\frac{\left(x-x_0\right)^2}{2\sigma_0^2+4Dt}\right), \qquad (2)$$

where x_0 is the depth of maximum concentration, and σ_0 can be derived either:

- from the full width at half maximum (FWHM) parameter of the implanted profile using

$$\sigma_0=\frac{\mathrm{FWHM}}{2\sqrt{2\ln(2)}}, \qquad (3)$$

or

- from the maximum concentration $C_{\max}$ and the fluence Q using

$$\sigma_0=\frac{Q}{\sqrt{2\pi}\,C_{\max}}. \qquad (4)$$

In summary, x_0 defines how far from the surface the initial hydrogen content is present, and σ_0 describes its Gaussian shape.

However, the experimental hydrogen concentration profiles depicted in Fig. 3 differ diametrically from those shown in Figs. 1 and 2.

At the outset, we observe that after annealing at 300°C, the maximum concentration of hydrogen increases, and the FWHM of the concentration profile decreases. This results from the low hydrogen solubility in zinc oxide and the relatively low diffusivity at temperatures of 300°C. The analyzed species segregate mostly in the region of the highly defective part of the material, and only a low amount of hydrogen diffuses outside the initial profile. Annealing at a temperature elevated up to 600°C leads to the removal of hydrogen atoms from their initial position, and the concentration profiles show a decrease in the initial concentration of over one order of magnitude, along with an increase in hydrogen concentration outside the hydrogen peak. There is also a noticeable difference between the H concentration in the direction towards the surface and towards the deeper part of the material. Similar behavior of hydrogen was observed in SiC [35]. This indicates a different solid solubility of hydrogen in the radiated part of the sample and in the non-radiated, deeper part. This difference may be due to defects, but is more likely due to differences in the carrier concentration (thus the Fermi level) in both parts of the sample. This results in a different energy formation of interstitial hydrogen and, ultimately, a different solubility of the species [36]. Taking into account the calculation done by Van de Walle [36], hydrogen acts as a donor for any Fermi level position in the ZnO band gap. The formation energy of H_i, and thus the solubility, decreases with an increase of the Fermi level. The concentration profile, as measured after annealing at 600°C for 30 min, confirms the inequality of hydrogen concentration on both sides of the original profile, with a higher concentration near the surface. Finally, both values of hydrogen content fit well with the hydrogen solubility calculated based on the solubility parameters from [4], giving 5.4×10^{17} cm^{-3} at 600°C.

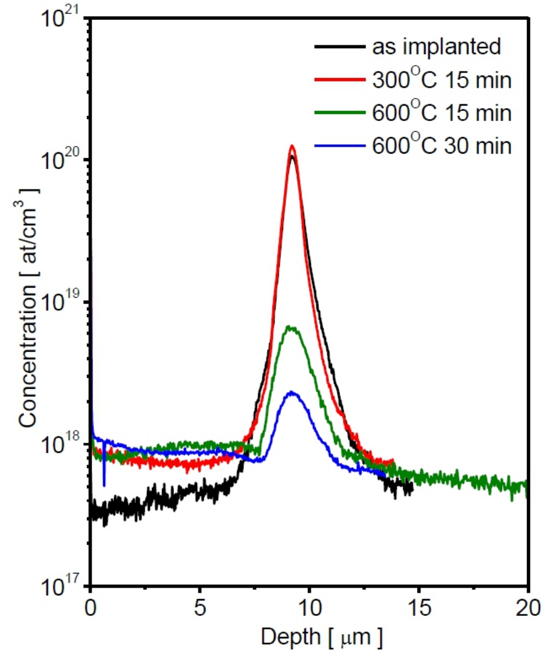

Fig. 3. Hydrogen concentration profiles obtained using the SIMS method.

Due to hydrogen segregation at 300°C, it is impossible to precisely calculate the diffusion coefficient at this temperature. It is also challenging to use the Gaussian fitting described above to the hydrogen concentration profile. Because of the low solid solubility of hydrogen at the studied temperature, the conditions allow us to treat the initial amount of species as an infinite source. Then, the lower detection limit of hydrogen could reveal two different erfc-like concentration profiles of diffused species (Fig. 3).

However, using the results for two different annealing times (15 and 30 min), we can estimate the diffusion coefficient at 600°C, taking into account the amount of hydrogen removed from the material during diffusion and the erf-like behavior of the diffused species. We can then use a semi-infinite model with a perfectly absorbing surface, which describes the amount of species transferred outside the sample through the surface. The amount of the remaining hydrogen is then represented by

$$Q\left(x,t\right)=\int_0^{\infty}\mathrm{d}x\;A\,\mathrm{erf}\left(\frac{x}{2\sqrt{D\,t}}\right). \qquad (5)$$

Taking into account the initial hydrogen fluence $Q = 10^{16}$ at/cm^2, the remaining amounts of hydrogen after 15 and 30 min of annealing are 21.4% and 11.7%, respectively. This ultimately results in the diffusion coefficient of 4.98×10^{-9} cm^2/s and 8.71×10^{-9} cm^2/s for 15 and 30 min, respectively. The average result ($\sim 6 \times 10^{-9}$ cm^2/s) is within the range of the diffusion coefficient for 600°C calculated by Ip et al. [15].

4. Conclusions

Hydrogen in ZnO was found to be highly mobile yet only sparingly soluble; therefore, post-implantation annealing produced a non-Gaussian profile evolution inconsistent with classical self-similar Fickian broadening. Areal-loss analysis for a semi-infinite solid with a perfectly absorbing surface enabled extraction of diffusion parameters without assuming a Gaussian initial and final profiles. From 15- and 30-min datasets at 600°C, a diffusion coefficient of $\sim 6 \times 10^{-9}$ cm^2/s was obtained. Process control is constrained by rapid out-diffusion; predictive modeling must include surface exchange and trapping, and the integrated-dose ratio is recommended as a robust metric for parameter extraction. Limitations include the perfect-sink assumption (i.e, a lower bound for the diffusion coefficient when surface exchange is finite) and SIMS uncertainties. Future work should determine E_a and D_0 based on a temperature span and incorporate a finite surface rate boundary to co-extract surface kinetics.

References

[1] C. Van de Walle, *Phys. Rev. Lett.* **85**, 1012 (2000).

[2] S.F.J. Cox, E.A. Davis, S.P. Cottrell et al., *Phys. Rev. Lett.* **86**, 2601 (2001).

[3] E. Mollwo, *Z. Phys.* **138**, 478 (1954).

[4] D.G. Thomas, J.J. Lander, *J. Chem. Phys.* **25**, 1136 (1956).

[5] J. Koßmann, C. Hattig, *Phys. Chem. Chem. Phys.* **14**, 16392 (2012).

[6] H.-H. Nahm, C.H. Park, Y.-S. Kim, *Sci. Rep.* **2**, 4124 (2014).

[7] Z.Q. Chen, A. Kawasuso, Y. Xu, H. Naramoto, X.L. Yuan, T. Sekiguchi, R. Suzuki, T. Ohdaira, *Phys. Rev. B* **71**, 115213 (2005).

[8] S.G. Koch, E.V. Lavrov, J. Weber, *Phys. Rev. B* **89**, 235203 (2014).

[9] W. Beyer, U. Breuer, F. Hamelmann, J. Hüpkes, A. Stärk, H. Stiebig, U. Zastrow, *Mater. Res. Soc. Symp. Proc.* **1165**, M05-24 (2009).

[10] Z. Zhou, K. Kato, T. Komaki, M. Yoshino, H. Yukawa, M. Morinaga, *Int. J. Hydrogen Energy* **29**, 323 (2004).

[11] M.D. McCluskey, S.J. Jokela, W.M. Hlaing, *Physica B* **376**, 690 (2006).

[12] E. Guziewicz, W. Woźniak, S. Mishra, R. Jakieła, M. Guziewicz, V.Y. Ivanov, E. Łusakowska, R. Schifano, *Phys. Status Solidi A* **218**, 2000318 (2021).

[13] K. Ip, M.E. Overberg, Y.W. Heo, D.P. Norton, S.J. Pearton, C.E. Stutz, B. Luo, F. Ren, D.C. Look, J.M. Zavada, *Appl. Phys. Lett.* **82**, 385 (2003).

[14] E.V. Monakhov, J.S. Christensen, K. Maknys, B.G. Svensson, A.Yu. Kuznetsov, *Appl. Phys. Lett.* **87**, 191910 (2005).

[15] K. Ip, M.E. Overberg, Y.W. Heo, D.P. Norton, S.J. Pearton, S.O. Kucheyev, C. Jagadish, J.S. Williams, R.G. Wilson, J.M. Zavada, *Appl. Phys. Lett.* **81**, 3996 (2002).

[16] B. Theys, V. Sallet, F. Jomard, A. Lusson, J.-F. Rommelučre, Z. Teukam, *J. Appl. Phys.* **91**, 3922 (2002).

[17] K. Ip, M.E. Overberg, Y.W. Heo, et al., *Solid-State Electron.* **47**, 2255 (2003).

[18] M.-S. Oh, D.-K. Hwang, J.-H. Lim, Y.-S. Choi, S.-J. Park, *Appl. Phys. Lett.* **91**, 212102 (2007).

[19] M.G. Wardle, J.P. Goss, P.R. Briddon, *Phys. Rev. Lett.* **96**, 205504 (2006).

[20] J. Bang, K.J. Chang, *Appl. Phys. Lett.* **92**, 132109 (2008).

[21] N.H. Nickel, *Phys. Rev. B* **73**, 195204 (2006).

[22] J. Hu, H.Y. He, B.C. Pan, *J. Appl. Phys.* **103**, 113706 (2008).

[23] K.M.H. Johansen, J.S. Christensen, E.V. Monakhov, A.Yu. Kuznetsov, B.G. Svensson, *Mater. Res. Soc. Symp. Proc.* **1035**, L03-10 (2008).

[24] W.H. Doh, P.C. Roy, C.M. Kim, *Langmuir* **26(21)**, 16278 (2010).

[25] L. Vines, R. Schifano, M. Schofield, B.G. Svensson, *Phys. Scr.* **T148**, 014005 (2012).

[26] J.-K. Park, K.-W. Lee, C.-E. Lee, *Solid State Commun.* **165**, 19 (2013).

[27] J. Cízek, F. Lukác, M. Vlcek, O. Melikhova, F. Traeger, D. Rogalla, H.-W. Becker, *J. Alloys Compd.* **580**, S51 (2013).

[28] M.A. Motin, P.C. Roy, C.M. Kim, *Phys. Status Solidi B* **253(8)**, 1649 (2016).

[29] K.S. Chan, L. Vines, K.M. Johansen, E.V. Monakhov, J.D. Ye, P. Parkinson, C. Jagadish, B.G. Svensson, J. Wong-Leung, *J. Appl. Phys.* **114**, 083111 (2013).

[30] S. Nagar, S.K. Gupta, S. Chakrabarti, *J. Lumin.* **153**, 307 (2014).

[31] M.-H. Du, K. Biswas, *Phys. Rev. Lett.* **106**, 115502 (2011).

[32] R. Schifano, R. Jakieła, A. Galeckas, K. Kopalko, F. Herklotz, K.M.H. Johansen, L. Vines, *J. Appl. Phys.* **126**, 125707 (2019).

[33] R. Jakieła, *Acta Phys. Pol. A* **136**, 916 (2019).

[34] K.M. Johansen, J.S. Christensen, E.V. Monakhov, A.Yu. Kuznetsov, B.G. Svensson, *Appl. Phys. Lett.* **93**, 152109 (2008).

[35] A. Barcz, M. Kozubal, R. Jakieła, J. Ratajczak, J. Dyczewski, K. Golaszewska, T. Wojciechowski, G.K. Celler, *J. Appl. Phys.* **115**, 223710 (2014).

[36] C.G. Van de Walle, J. Neugebauer, *Nature* **423**, 626 (2003).